

University of Wollongong

Research Online

---

Faculty of Engineering and Information  
Sciences - Papers: Part B

Faculty of Engineering and Information  
Sciences

---

2019

## Characterization of prompt gamma ray emission for in vivo range verification in particle therapy: A simulation study

Melek Zarifi

*University of Wollongong, mz659@uowmail.edu.au*

Susanna Guatelli

*University of Wollongong, susanna@uow.edu.au*

Yujin Qi

*University of Wollongong, yujin@uow.edu.au*

David Bolst

*University of Wollongong, dbolst@uow.edu.au*

Dale A. Prokopovich

*Australian Nuclear Science and Technology Organisation, dalep@uow.edu.au*

*See next page for additional authors*

Follow this and additional works at: <https://ro.uow.edu.au/eispapers1>



Part of the [Engineering Commons](#), and the [Science and Technology Studies Commons](#)

---

### Recommended Citation

Zarifi, Melek; Guatelli, Susanna; Qi, Yujin; Bolst, David; Prokopovich, Dale A.; and Rosenfeld, Anatoly B., "Characterization of prompt gamma ray emission for in vivo range verification in particle therapy: A simulation study" (2019). *Faculty of Engineering and Information Sciences - Papers: Part B*. 2858. <https://ro.uow.edu.au/eispapers1/2858>

Research Online is the open access institutional repository for the University of Wollongong. For further information contact the UOW Library: [research-pubs@uow.edu.au](mailto:research-pubs@uow.edu.au)

---

# Characterization of prompt gamma ray emission for in vivo range verification in particle therapy: A simulation study

## Abstract

In this paper we investigate the emission and detection characteristics of prompt gamma (PG) rays for in vivo range verification during hadron therapy, using Geant4 simulations. Proton,  $^4\text{He}$  and  $^{12}\text{C}$  beams of varying energy are incident on water phantoms. The PG production yield, energy spectral characteristics and spatial correlation with the Bragg Peak (BP) have been quantified. Further, the angular distributions for PG detection with respect to a point-of-reference on the phantom surface have been explored. The temporal properties of PG emission and time-of-flight (TOF) of PG detection have also been investigated in correlation with the changing particle beam range. Our results show that the primary PG rays from nuclear interactions of the primary beam exhibit the closest correlation to the beam range but its signal is significantly masked by the concurrent secondary PG rays, particularly for heavier ions such as carbon ion beams. The PG TOF spectroscopy encodes the essential information of the beam range but requires high time resolution measurements to retrieve it. A hybrid PG detection system to utilize the energy, timing and spatial characteristics of PG rays is desirable for BP tracking in real-time.

## Disciplines

Engineering | Science and Technology Studies

## Publication Details

Zarifi, M., Guatelli, S., Qi, Y., Bolst, D., Prokopovich, D. & Rosenfeld, A. (2019). Characterization of prompt gamma ray emission for in vivo range verification in particle therapy: A simulation study. *Physica Medica: an international journal devoted to the applications of physics to medicine and biology*, 62 20-32.

## Authors

Melek Zarifi, Susanna Guatelli, Yujin Qi, David Bolst, Dale A. Prokopovich, and Anatoly B. Rosenfeld

# Characterization of prompt gamma ray emission for *in vivo* range verification in particle therapy: A simulation study

Melek Zarifi<sup>a</sup>, Susanna Guatelli<sup>a</sup>, Yujin Qi<sup>a</sup>, David Bolst<sup>a</sup>, Dale Prokopovich<sup>b</sup>, Anatoly Rosenfeld<sup>a\*</sup>

<sup>a</sup>Centre for Medical Radiation Physics, University of Wollongong, NSW, Australia

<sup>b</sup>Australian Nuclear Science and Technology Organization, Lucas Heights, NSW, Australia

\*Corresponding Author: Anatoly Rosenfeld, email: anatoly@uow.edu.au

## Abstract

In this paper we investigate the emission and detection characteristics of prompt gamma (PG) rays for *in vivo* range verification during hadron therapy, using Geant4 simulations. Proton, <sup>4</sup>He and <sup>12</sup>C beams of varying energy are incident on water phantoms. The PG production yield, energy spectral characteristics and spatial correlation with the Bragg Peak (BP) have been quantified. Further, the angular distributions for PG detection with respect to a point-of-reference on the phantom surface have been explored. The temporal properties of PG emission and time-of-flight (TOF) of PG detection have also been investigated in correlation with the changing particle beam range. Our results show that the primary PG rays from nuclear interactions of the primary beam exhibit the closest correlation to the beam range but its signal is significantly masked by the concurrent secondary PG rays, particularly for heavier ions such as carbon ion beams. The PG TOF spectroscopy encodes the essential information of the beam range but requires high time resolution measurements to retrieve it. A hybrid PG detection system to utilize the energy, timing and spatial characteristics of PG rays is desirable for BP tracking in real-time.

Keywords: Prompt Gamma, Range Verification, Bragg Peak Tracking, Hadron Therapy, Time-of-Flight

## 1. Introduction

The goal of radiation therapy is to deliver highly localized treatment dose to kill cancer cells in the tumor volume while protecting the surrounding healthy tissue from radiation damage as much as possible. Hadron therapy (HT), based on charged particle beams such as proton (<sup>1</sup>H), helium (<sup>4</sup>He) and carbon (<sup>12</sup>C), offers unique benefits for cancer treatment over conventional photon therapy [1]. Most of the energy from hadron beams is deposited in the sharp and narrow Bragg Peak (BP) at the end of their range, which allows for a precise local dose distribution in the target tumor volume while minimizing the overspill of radiation on the healthy tissue. An additional advantage of HT is the enhanced relative biological effectiveness (RBE) of heavy ions, which is particularly beneficial for the treatment of radio-resistant or pediatric tumors [2]. However, the ability to fully exploit the advantages of HT is still limited by various uncertainties in predicting and determining the beam's range in the traversed tissues [3]. The beam range uncertainties significantly affect the achievable treatment precision and lead to clinical applications with conservative safety

margins [4]. *In vivo* range verification and dose monitoring in real-time are desired to ensure high quality HT treatment, but such experimental tools remain unavailable in clinical routine.

The promising strategy for *in vivo* beam range verification is to make use of the by-products of secondary penetrating radiations that occur during irradiations since the primary beam is absorbed inside the patient, such as interaction vertex imaging (IVI) [5], secondary electron bremsstrahlung (SEB) [6], thermoacoustic waves [7] and high energy gamma rays produced by hadronic beam interactions with tissue nuclei [8]. Over the past decades, significant research efforts have been undertaken worldwide to develop *in vivo* beam range verification techniques using the secondary radiation emission of gamma rays [9,10]. Positron emission tomography (PET) has been adopted for HT monitoring in clinical application. It relies on detecting and imaging the positron-annihilation photons occurring from the decay of positron emitters created as a result of beam nuclear interactions with tissue nuclei [11-13]. However, the delayed decay of the short-lived radioisotopes, on the order of 1-20 minutes with respect to the irradiation, presents a major limitation for beam range verification in real-time. The quantitative accuracy of beam range verification from PET is also limited by a relatively low photon yield, the positron range effect and the biological washout effect. Furthermore, the production of the PET isotopes does not occur within the BP and requires some form of deconvolution to reconstruct the BP. On the other hand, the emission of prompt gamma (PG) rays from the decay of excited nuclear reaction products takes place almost instantaneously with the beam irradiation, thus allowing for BP tracking in real-time during treatment delivery with no washout effect [14]. The PG signal has been considered as the most desirable means for real-time *in vivo* range verification. However, the PG signal is largely masked by the concurrent emission of secondary PG rays resulting from the nuclear reactions undergone by the secondary particles/fragments created along the primary ion beam path, which could affect the accuracy of the BP tracking. This effect would be more pronounced with heavier ion species such as carbon beams with higher energies.

PG emissions present several distinctive characteristics in space, energy and timing that have been proposed for *in vivo* range verification. The methods and feasibility of employing PG rays for beam range verification have been intensively studied for proton [15,16] and carbon beams [17,18], and recently reviewed in [19]. Helium ions for HT have gained increasing interest for clinical applications as the recent dosimetry characteristics studies of helium ions show that it could offer a more conformal treatment and in turn increase tumor control [20-22]. However, the PG emission characteristics from helium irradiation have not yet been widely studied [23]. The spatial correlation between PG rays and the depth dose profile has resulted in PG imaging (PGI) methods, including mechanical collimation such as slit cameras [24-26] and electronic collimation such as Compton cameras [27-29]. Recent clinical trials with the IBA knife-edge slit camera on patients [30,31] demonstrated that millimeter-level accuracy is achievable. Xie et al 2017 [31] demonstrated that PGI for *in vivo* proton beam range verification in actively delivered pencil beam scanning (PBS) on spot-by-spot tracking is feasible. However, the count statistics is still one of the main issues in such systems to achieve higher statistical precision of *in vivo* beam range verification. The slit camera based system can only provide one-dimensional

range information in the longitudinal beam direction but lacks the lateral spread information. Compton cameras could offer the possibility to perform 2D or 3D imaging but suffer high technological challenges in detectors and image reconstruction to achieve clinically acceptable images [32]. Other methods based on specific counting to utilize either the characteristic PG spectroscopy (PGS) [33,34], PG timing (PGT) [35] or PG peak integration (PGPI) [36], have recently been proposed as alternatives to the PGI. These non-imaging approaches have an advantage with low footprint detector setup in clinical practice. Each of these methods has its own advantages and shortcomings. Hybrid PG detection methods may be necessary to overcome the challenges of a broad- and high-energy distribution, a large background, high instantaneous count rates, and compatibility constraints with patient irradiation. This requires systematic studies of the PG characteristics in space, energy and time.

A recent breakthrough of clinical prototype for proton range verification has been reported from the Massachusetts General Hospital (MGH) group [37]. It utilized energy- and time-resolved spectral measurements of PG rays with slit collimation and integrated with a Monte Carlo simulation based treatment planning system. The system can verify the absolute range of proton pencil beams with high spatial precision (1.1 mm) in phantoms under realistic clinical conditions. However, in this approach the temporal PGT information was only used to reject the gamma ray background from proton-induced and neutron-induced continua. The PGT information could be further utilized with hybrid PG detection systems for beam range verification.

In this work, we focus on investigating the global properties of PG ray emission and propagation in a water phantom for *in vivo* range verification in HT for three different ion species: protons, helium and carbon ions. The PG production and detectable yields, and its emission distribution relationship with the dose distribution are quantified as a function of ion beam energies. The temporal properties of PG emission and time-of-flight (TOF) for detection are also explored to characterize the associated correlation with the changing particle beam range. This study not only compares the three ion species relevant to HT applications but also aims to optimize detection parameters, presenting also several quantitative data of PG emission and global detection. Hence, this paper will provide valuable information for designing an optimal PG detector system to allow accurate and efficient PG measurements for *in vivo* beam range monitoring in real-time.

## 2. Methods

The Geant4 Monte Carlo Toolkit [38-40] (version 10.02 patch 02) was used to investigate the characteristic emission of PG rays from the particle beams under study, incident on a homogeneous water phantom (density of 1 g/cm<sup>3</sup>). The set-up of the simulation is shown in Figure 1. Mono-energetic pencil beams of proton, <sup>4</sup>He and <sup>12</sup>C ions were used to irradiate spherical phantoms of 40 cm diameter, with the beam axis crossing the centre of the phantom (see Figure 1). The size of the phantom was chosen to represent the size of a human abdomen, and for simplicity, a spherical shape is used. The energy deposited in the phantom was calculated along the direction of incidence of the beam (z-axis) so to obtain particle depth dose curves. The bin size of the depth dose profile

is 1 mm. The energy deposited along the x-axis at the position of the BP, for a longitudinal width of 10 mm, was also calculated. Proton and  $^4\text{He}$  beams of 62, 150, 200 and 250 MeV/u, and  $^{12}\text{C}$  beams of 120, 285, 385 and 490 MeV/u were simulated. From our simulation results, these energies correspond to ranges (80% distal dose fall-off) of approximately 30, 160, 260 and 380 mm in water. The beam range values are consistent with NIST [41] for proton/helium ions and SRIM [42] for carbon ions taking into account that they calculate the ranges with the continuous slowing down approximation (CSDA) and projected range algorithm (PRAL), respectively. These energy ranges were chosen as they are typical of therapy treatment for the respective particle types with the exception of the energies 250 MeV/u of  $^4\text{He}$  and 490 MeV/u of  $^{12}\text{C}$ , which were also included for comparison. The number of incident particles was  $10^8$  for protons,  $10^7$  for  $^4\text{He}$  ions and  $10^6$  for  $^{12}\text{C}$  ions to obtain a statistical uncertainty of 5% in the yield of PG rays. The statistical uncertainty was calculated with  $1/\sqrt{N}$ , where  $N$  is the number of counts. Uncertainties that affect physics concepts are not taken into account, the uncertainties are purely statistical. An air-filled idealized detecting sphere surface (called *detection sphere*), with 100 cm diameter encompassing the phantom, was used to score the gamma rays and neutrons reaching its surface once emitted from the phantom. Characterization of the gamma/neutron radiation field using the detection sphere provides beneficial information which assists in choosing potential PG detectors. As the BP position within the phantom varies with particle beam energy, a fixed point of reference was chosen at the surface of the phantom, which is similar to a fixed point on the patient surface in the clinical setting. Hence, the simulation coordinate centre was fixed at the surface of the phantom and at the centre of the detection sphere.

A modularized Geant4 Physics List was used which included both electromagnetic (*G4EmStandardPhysics\_option3*) and hadronic physics (*QGSP\_BIC\_HP*). The *G4RadioactiveDecayPhysics* and *G4HadronElasticPhysicsHP* modules were active. The *QGSP\_BIC\_HP* was chosen as it was found adequate for proton and carbon therapy studies in [43,44]. Total cross sections are described by the Glauber-Gribov theory [45] and the final state of inelastic scattering is generated by the Binary Cascade model [46]. The High Precision Neutron Data Libraries were used to more accurately model the neutron interactions from thermal energies up to 20 MeV. Recent efforts to assess and improve the accuracy of prompt gamma productions in Geant4 physics for HT have been reported [47,48].

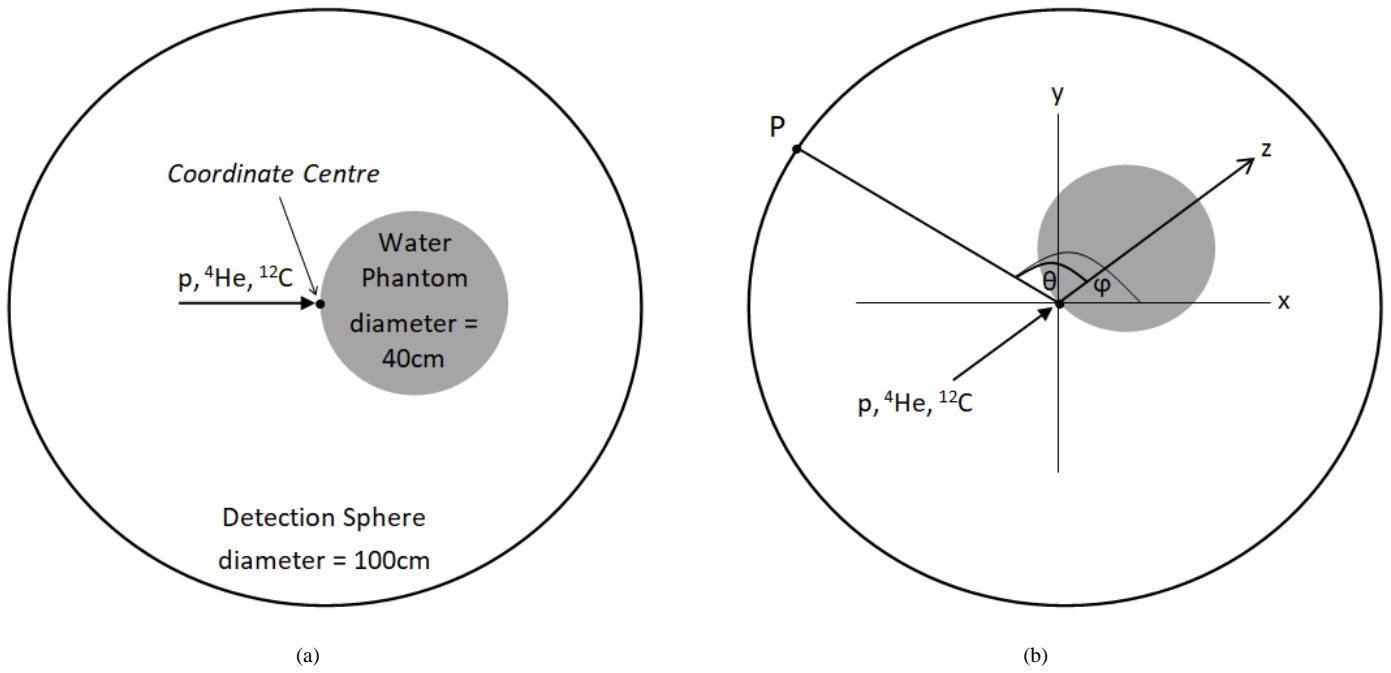


Figure 1 (a) Geometrical simulation setup of the spherical water phantom in an air-filled detection sphere. (b) The angle  $\theta$  is formed from the longitudinal beam direction (z-axis) with the centre of the coordinate system at the phantom surface. P is the PG detection position on the detection sphere traversed by the photons, and  $\varphi$  is the azimuthal angle.

The output of the simulation consisted of the emission yield of the secondary photons and neutrons when they originate in the phantom, and when they reach the detection sphere. The emission yield was normalized to the number of incident particles on the phantom. The PG emission time was calculated as the time interval between the origin of the primary particle in the simulation and the time of origin of the PG ray in the phantom. The PG detection time, defined as TOF, was calculated as the time interval between the origin of the primary particle in the simulation and the time when the PG ray reaches the detection sphere. The gamma TOF distribution mean and integral were retrieved from the simulation.

In the post-simulation data analysis, several parameters of PG emission and detection were investigated. Table 1 lists these variables and their definition in this study.

Table 1. Variables and definitions.

Variable	Definition
R	Particle beam range, defined as the position with 80% BP distal fall-off along the beam path in the phantom
$R_{PG}$	PG range, defined as the position with 80% PG emission yield fall-off in the phantom
$\Delta_{fall-off}$	The difference $R - R_{PG}$ , used to quantify the longitudinal correlation between the PG emission and the beam range
$\Delta_{FWHM}$	The difference between the lateral PG emission distribution FWHM and lateral dose distribution FWHM for a 10 mm longitudinal thickness at the BP position
$T_{PG}$	The 80% fall-off of the PG emission time distribution
$T_w$	The time difference between 80% rise and fall-off of the TOF spectra peak

In considering a point-of-reference in clinical conditions, the centre of the simulation coordinate system was fixed at the surface of the phantom, corresponding to the point of beam incidence. The angular emission characteristics of PG rays were studied with the polar angle  $\theta$  formed from the longitudinal beam direction (z-axis) with the point-of-reference (see Figure 1 (b)). The polar angle allows one to explore PG emission and propagation in the phantom and investigate a potential preferential position defined with respect to the surface of the phantom, where to locate the detector/s to maximize the number of detected PG rays.

All photons generated in the water phantom, via any physical interaction process, were retrieved by the simulation. The energy spectrum of these photons allowed the observation of the prominent PG emission lines and the selection of two energy windows to study their yield and spatial correlation with respect to the BP, and their temporal and detection properties. The first energy selection had a threshold of  $\geq 1$  MeV, which eliminates the low-energy background photon counts [49], and the second had a 3.0-7.0 MeV window, which includes the prominent PG emission lines and has been employed in previous studies [50,51]. The primary PG rays are referred to those produced from the primary particle beam interactions, and the secondary PG rays are referred to those produced from the interactions of the secondary radiation field. In addition, when calculating the PG emission yield to deposited energy ratio for the different ion species, we take the energy deposited and scored at the BP maximum.

### 3. Results

#### 3.1 Energy spectra of prompt gamma emission within the water phantom

Figure 2 shows the energy spectra of photons that originate in the water phantom from any physical interaction (including gamma photons induced by neutrons) for the three beam particle types. In each case the energy spectra show a consistent shape over a wide energy range, with several characteristic emission lines produced by non-elastic particle-nuclei interactions with major constituent elements of the phantom material. A peak at 0.511 MeV originates from the annihilation of positrons resulting from the decay of  $^{15}\text{O}$  and  $^{11}\text{C}$  nuclei among other isotopes that are also produced and contribute to this peak. The 2.22 MeV peak is a result of secondary thermal neutron capture by hydrogen nuclei. A 2.3 MeV peak arises from  $^{14}\text{N}$  by proton and alpha spallation reactions with  $^{16}\text{O}$  [52], which may be difficult for a detector to resolve from the 2.22 MeV neutron capture line. The prominent PG emission lines are observed with energy 4.44, 5.21 and 6.13 MeV, which are the most adopted PG rays for beam range verification. The 4.44 MeV PG emission line originates from the de-excitation of  $^{12}\text{C}^*$  nuclei, derived from particle nuclear interactions with oxygen nuclei. The 5.21 and 6.13 MeV PG emission lines arise from  $^{15}\text{O}^*$  and  $^{16}\text{O}^*$  de-excitations, respectively. The intensity of the 2.3 MeV peak is comparable to the 4.44, 5.21 and 6.13 MeV peaks, however it could be challenging to detect since the 2.3 MeV line could be merged with the neutron capture line and detection will depend on the energy resolution of the detector. Hence, for this study we keep an energy window option for PG selection from 3.0 to 7.0 MeV, since it contains the most adopted PG emission lines for range verification for potential comparison purposes, as well as containing the 6.13 MeV line from



oxygen which is the most abundant element in the human body. In addition, the energy threshold of  $\geq 1$  MeV eliminates background photon counts, particularly those resulting from positron annihilation. The potential utilizable PG line at 0.718 MeV was not included in our simulation since it may be difficult to resolve in some detectors, such as LYSO detectors, where detector intrinsic radioactivity may interfere with the PG signal.

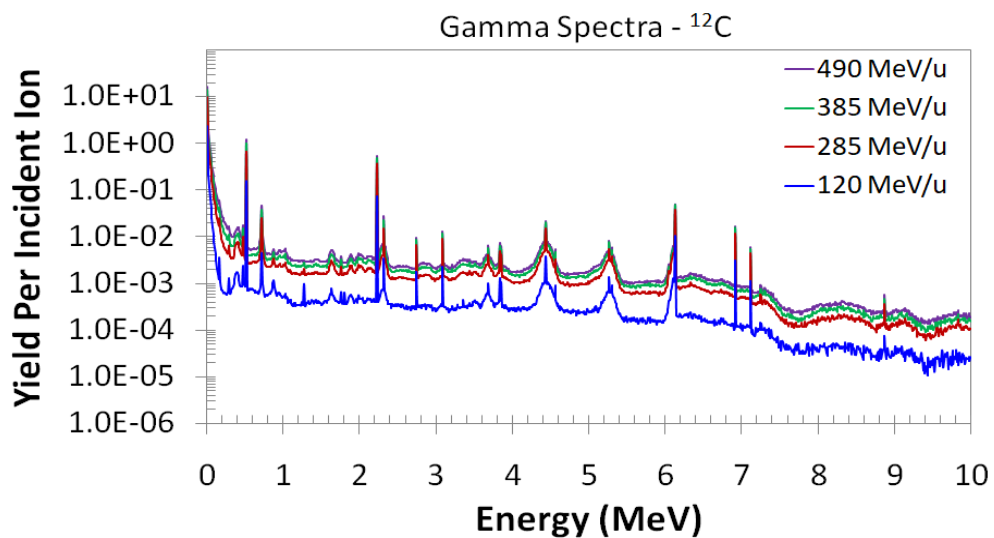
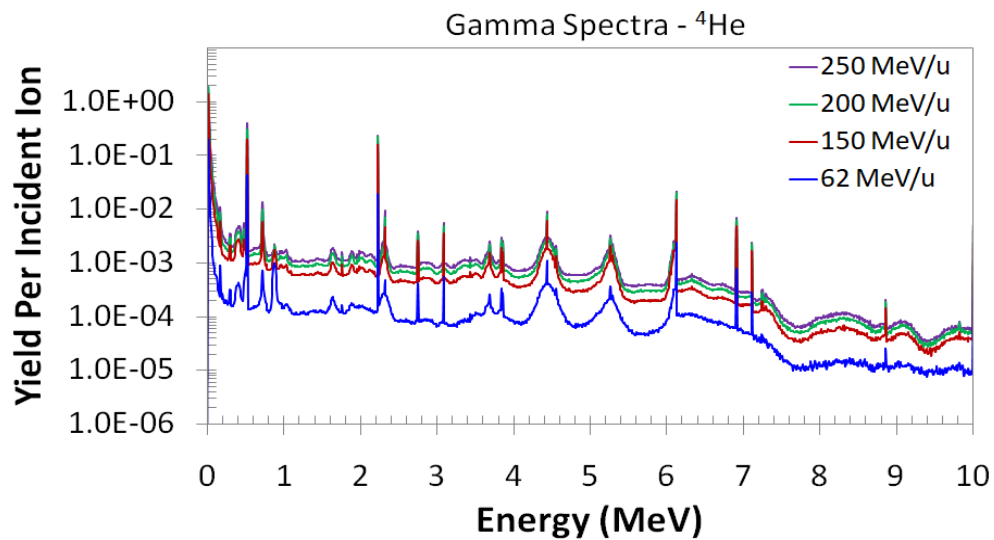
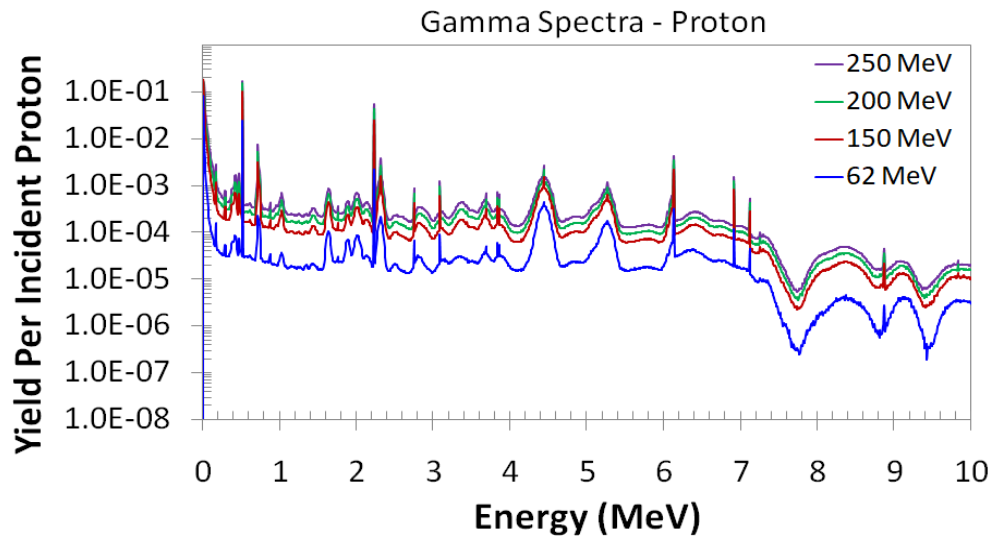
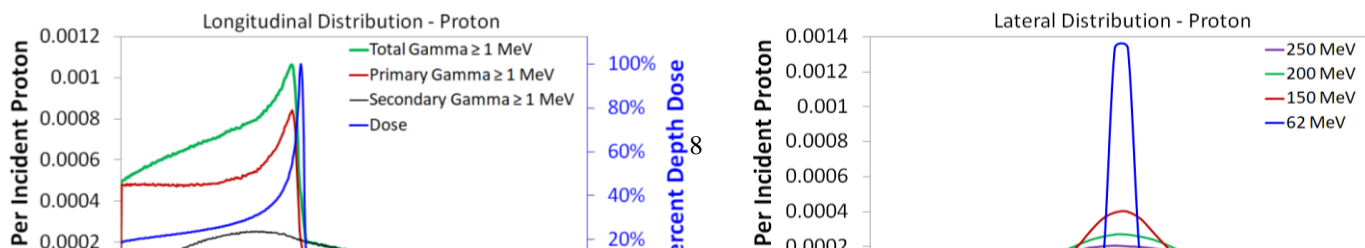


Figure 2. Energy spectra of photons generated in the water phantom deriving from pencil beams of protons,  $^4\text{He}$  and  $^{12}\text{C}$  ions. The emission lines are characteristic to the major constituent elements of the phantom material. The distinctive PG emission lines of energy 4.44, 5.21 and 6.13 MeV result from  $^{12}\text{C}$ ,  $^{15}\text{O}$  and  $^{16}\text{O}$  nuclear de-excitations, respectively.

### 3.2 Spatial correlation between prompt gamma emission and the particle beam range

Figure 3 shows the longitudinal and lateral distribution of gamma rays produced in the phantom. The Bragg curve (for ~16 cm range) is plotted with the longitudinal distribution to show the correlation between the gamma emission and the dose deposition. It can be observed that the primary PG profile shows the closest correlating relationship to the beam range regarding the sharpness and fall-off in the BP region, which can provide reliable BP tracking in HT. The secondary PG profile shows a broad distribution with a long tail beyond the BP downstream, which could cause significant interference on the BP tracking. The secondary PG productions become more dominant in heavier ions (helium and carbon) than that in proton beams. In the PG emission of  $^4\text{He}$  and  $^{12}\text{C}$  a discontinuity can be seen, which may be due to the transition to the precompound model at low energy nuclear reactions. The transition between high- and low-energy nuclear reaction models occurs at around 140 mm for  $^4\text{He}$  and at around 160 mm for  $^{12}\text{C}$ . The lateral spreads of PG emissions are broader with increasing beam energies. The heavier ion beam (carbon) shows narrower lateral spread of PG emissions than the proton beam. This trend is consistent with that in their lateral dose spreads.



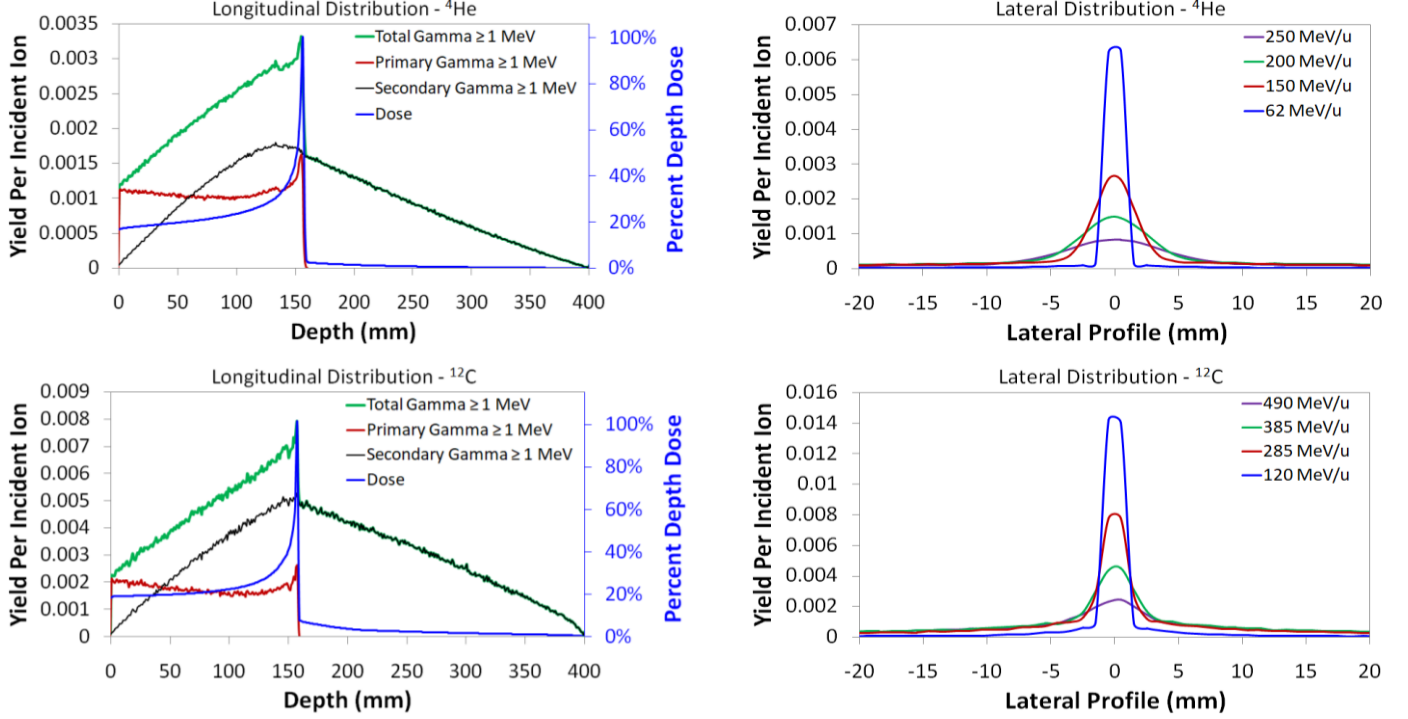


Figure 3. Left: Longitudinal yield distribution of total, primary and secondary gamma rays  $\geq 1$  MeV originating in the water phantom for protons (150 MeV),  $^4\text{He}$  (150 MeV/u) and  $^{12}\text{C}$  (285 MeV/u) ions. The percent depth dose is normalized to the dose maximum at the Bragg Peak. Right: Lateral yield distribution of total gamma rays  $\geq 1$  MeV for a longitudinal width of 10 mm at the BP positions for each of the beam energies.

Table 2 presents data for the particle range and corresponding PG range for the applied energy threshold and window, for each incident particle type and energy under investigation. The quantified longitudinal difference,  $\Delta_{fall-off}$ , shows that the PG rays within 3.0-7.0 MeV offer better correlation to the beam range, particularly in the case of incident protons. For a particle range at 16 cm depth, the  $\Delta_{fall-off}$  values are  $(-5.1 \pm 0.5)$  mm,  $(+0.2 \pm 0.5)$  mm and  $(+0.3 \pm 0.5)$  mm, for proton,  $^4\text{He}$  and  $^{12}\text{C}$  ions, respectively. Negative  $\Delta_{fall-off}$  values indicate that the PG range is upstream of the particle range, while positive values indicate downstream of the particle range. However, the energy window offers the lowest gamma statistical yield (see Table 3). Instead the threshold of gamma rays  $\geq 1$  MeV, which eliminates low-energy background counts while incorporating the prominent PG rays, offers a good PG-BP position correlation with the benefit of a higher yield. It can be seen that for helium and carbon ions the variation of accuracy ( $\Delta_{fall-off}$ ) is relatively small across the particle beam energies, independently from the gamma energy

windows, with an improved accuracy in estimating the beam range for these heavier ions with respect to incident protons. The quantified difference,  $\Delta FWHM$ , shows that there is good conformity between the lateral PG production and dose deposition.

Table 2. Particle beam range and corresponding PG range for the applied energy threshold and window studied, for each particle beam type and energy. The  $\Delta fall-off$  and  $\Delta FWHM$ , defined in Section 2, are reported for quantitative evaluation.

Particle Type	Beam Energy (MeV/u)	Gamma Energy Selection (MeV)	Longitudinal Beam Range ( $\pm 0.5$ mm)	Longitudinal PG Range ( $\pm 0.1$ mm)	$\Delta fall-off^*$ ( $\pm 0.5$ mm)	Lateral Dose FWHM ( $\pm 0.2$ mm)	Lateral PG FWHM ( $\pm 0.2$ mm)	$\Delta FWHM$ ( $\pm 0.3$ mm)
Proton	62	$\geq 1$	31.9	27.0	-4.9	1.2	1.0	0.2
		3.0-7.0		27.2	-4.7		1.0	0.2
	150	$\geq 1$	155.5	150.2	-5.3	7.1	6.7	0.4
		3.0-7.0		150.4	-5.1		6.7	0.4
	200	$\geq 1$	256.3	250.8	-5.5	11.9	11.8	0.1
		3.0-7.0		251.4	-4.9		11.4	0.5
250	$\geq 1$	374.7	368.2	-6.2	17.5	16.4	1.1	
	3.0-7.0		369.6	-5.1		16.6	0.9	
<sup>4</sup> He	62	$\geq 1$	32.2	31.8	-0.4	0.7	0.6	0.1
		3.0-7.0		32.0	-0.2		0.6	0.1
	150	$\geq 1$	156.6	156.6	0.	3.5	3.6	0.1
		3.0-7.0		156.8	+0.2		3.5	0.
	200	$\geq 1$	258.2	258.3	+0.1	5.9	6.3	0.4
		3.0-7.0		258.4	+0.2		6.1	0.2
250	$\geq 1$	377.4	377.4	0.	8.5	9.0	0.5	
	3.0-7.0		377.4	0.		9.4	0.9	
<sup>12</sup> C	120	$\geq 1$	35.2	35.5	+0.3	0.3	0.4	0.1
		3.0-7.0		35.4	+0.2		0.4	0.1
	285	$\geq 1$	157.3	157.8	+0.5	1.9	2.0	0.1
		3.0-7.0		157.6	+0.3		1.8	0.1
	385	$\geq 1$	257.5	258.7	+1.2	3.1	3.4	0.3
		3.0-7.0		258.3	+0.8		3.3	0.2
490	$\geq 1$	377.7	378.7	+1.0	4.5	5.2	0.7	
	3.0-7.0		378.6	+0.9		4.8	0.3	

\* Negative values indicate that the PG range is upstream of the particle range, while positive values indicate downstream of the particle range.

### 3.3 Prompt gamma emission and detectable yield

The yield values of PG rays originating in the spherical water phantom per incident particle are estimated and listed in Table 3. In the same table, the yields of PG rays reaching the detection sphere are reported. For each beam type, the PG emission yield increases with greater particle energy, as expected. The <sup>12</sup>C beam produces the highest yield of gamma emission compared to the proton and <sup>4</sup>He beams, with a relatively larger yield of low-energy photon counts. For example, comparing the beam types with

the same range of about 16 cm, the total gamma yield per incident particle is 0.87 for 150 MeV protons, 2.60 for 150 MeV/u  $^4\text{He}$  ions and 17.35 for 285 MeV/u  $^{12}\text{C}$  ions, while the yield for PG rays within 3.0-7.0 MeV is 0.07, 0.22 and 0.62, respectively. This gives a ratio of total gamma to PG of 12.4, 11.8 and 28.0 for proton,  $^4\text{He}$  and  $^{12}\text{C}$ , respectively. In other words, for 150 MeV protons the energy deposited at the BP maximum is  $\sim 3$  MeV/ion, with a PG yield of  $\sim 7 \times 10^{-4}$  /ion, which corresponds to  $\sim 2 \times 10^{-4}$  PG rays emitted per MeV deposited energy at the BP. For 150 MeV/u  $^4\text{He}$  ions the energy deposited at the BP maximum is  $\sim 13$  MeV/ion, with a PG yield of  $\sim 1 \times 10^{-3}$  /ion, and  $\sim 8 \times 10^{-5}$  PG/MeV at the BP. For 285 MeV/u  $^{12}\text{C}$  ions the energy deposited at the BP maximum is  $\sim 69$  MeV/ion, with a PG yield of  $\sim 4 \times 10^{-3}$  /ion, and  $\sim 6 \times 10^{-5}$  PG/MeV at the BP.

As expected, the detectable photon yield is less than the emission yield, since the gamma rays interact within the water phantom and can eventually be absorbed. The detectable PG (3.0-7.0 MeV) yield on the detection sphere is found to be around 65%. Again, the results show that the  $^{12}\text{C}$  beam produces a higher yield of detectable PG rays per incident ion compared to the proton and  $^4\text{He}$  beams. The PG yield, between 3.0-7.0 MeV, per incident particle for the beams with around 16 cm range is 0.05 for protons (150 MeV), 0.14 for  $^4\text{He}$  (150 MeV/u) ions and 0.40 for  $^{12}\text{C}$  (285 MeV/u) ions.

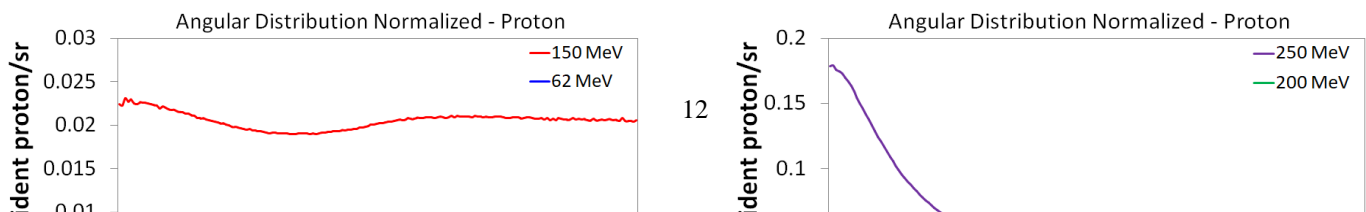
Table 3. Yield values of gamma photons originating within the water phantom and those reaching the detection sphere once emitted from the phantom. The simulation statistical uncertainty is within 5%.

Particle Type	Particle Beam Energy (MeV/u)	Gamma Energy Selection (MeV)	Gamma Yield Per Incident Particle	
			In Phantom	Detection Sphere
Proton	62	No window	0.19	0.06
		$\geq 1$	0.03	0.02
		3.0-7.0	0.02	0.01
	150	No window	0.87	0.25
		$\geq 1$	0.13	0.09
		3.0-7.0	0.07	0.05
	200	No window	1.40	0.39
		$\geq 1$	0.20	0.14
		3.0-7.0	0.10	0.07
	250	No window	1.95	0.53
		$\geq 1$	0.27	0.19
		3.0-7.0	0.13	0.09
$^4\text{He}$	62	No window	0.41	0.17
		$\geq 1$	0.10	0.08
		3.0-7.0	0.05	0.04
	150	No window	2.60	0.86
		$\geq 1$	0.54	0.36
		3.0-7.0	0.22	0.14
	200	No window	4.00	1.25
		$\geq 1$	0.77	0.51

		3.0-7.0	0.32	0.20
	250	No window	5.20	1.55
		$\geq 1$	0.90	0.61
		3.0-7.0	0.38	0.25
$^{12}\text{C}$	120	No window	3.91	0.73
		$\geq 1$	0.32	0.23
		3.0-7.0	0.15	0.10
	285	No window	17.35	2.94
		$\geq 1$	1.42	0.95
		3.0-7.0	0.62	0.40
	385	No window	25.02	4.25
		$\geq 1$	2.00	1.35
		3.0-7.0	0.86	0.56
	490	No window	30.40	5.42
		$\geq 1$	2.44	1.66
		3.0-7.0	1.01	0.67

### 3.4 Angular distribution for detectable prompt gamma

Figure 4 shows the angular distributions of total gamma rays which reach the idealized detection sphere normalized per incident ion per steradian for proton,  $^4\text{He}$  and  $^{12}\text{C}$  beams for the different beam energies. At the low energies of 62 MeV/u (for both proton and helium beams) and 120 MeV/u (for carbon beam), the detectable gamma rays are slightly preferred backward in  $\theta = 100-180^\circ$ . But at higher beam energies the detectable gamma emissions become more forward in  $\theta = 20-40^\circ$ . In addition, such forwardness increases with the heavier ion species. With increasing depth of the BP position as the beam energy increases, the favorable PG detection is likely to be increasingly forward. Further analysis of proton irradiations with respect to the BP position can be found in our previous study [53].



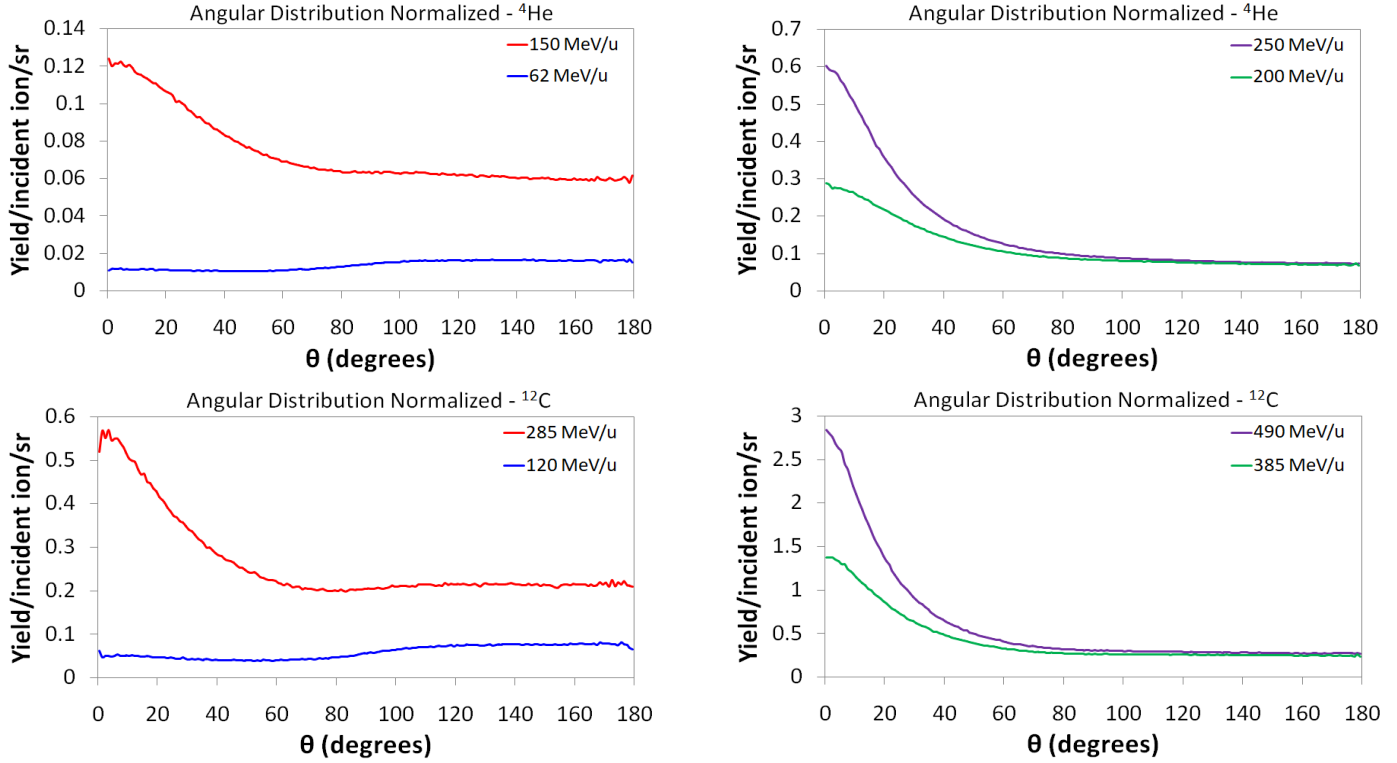


Figure 4. Angular distribution of total gamma rays reaching the idealized detecting sphere normalized per incident ion per steradian for the lower two beam energies (left) and the higher two beam energies (right) for protons,  ${}^4\text{He}$  and  ${}^{12}\text{C}$  ions.

### 3.5 Temporal characteristics of prompt gamma emission and detection: relationship with the particle beam range

The timing distribution of PG emission varies with particle beam energy as expected, since the beam range/transit time also increases and so gamma rays are produced at greater depths in the phantom and hence at later time. Figure 5 shows the emission time distribution of total gamma rays and those  $\geq 1$  MeV for each particle type and energy. The PG emission time profiles with applied gamma energy threshold of 1 MeV show a clear fall-off which is linked to the BP fall-off in the dose profile. The PG emission time  $T_{\text{PG}}$  (defined in Section 2) for gamma rays  $\geq 1$  MeV is  $(2.5 \pm 0.1)$  ns,  $(2.7 \pm 0.1)$  ns and  $(1.9 \pm 0.1)$  ns for protons,  ${}^4\text{He}$  and  ${}^{12}\text{C}$  ions with a range of around 38 cm. The emission time of gamma rays from carbon ions is seen to be quicker than that of proton and helium ions; this may be due to the carbon ions moving at greater speed as they traverse the phantom.

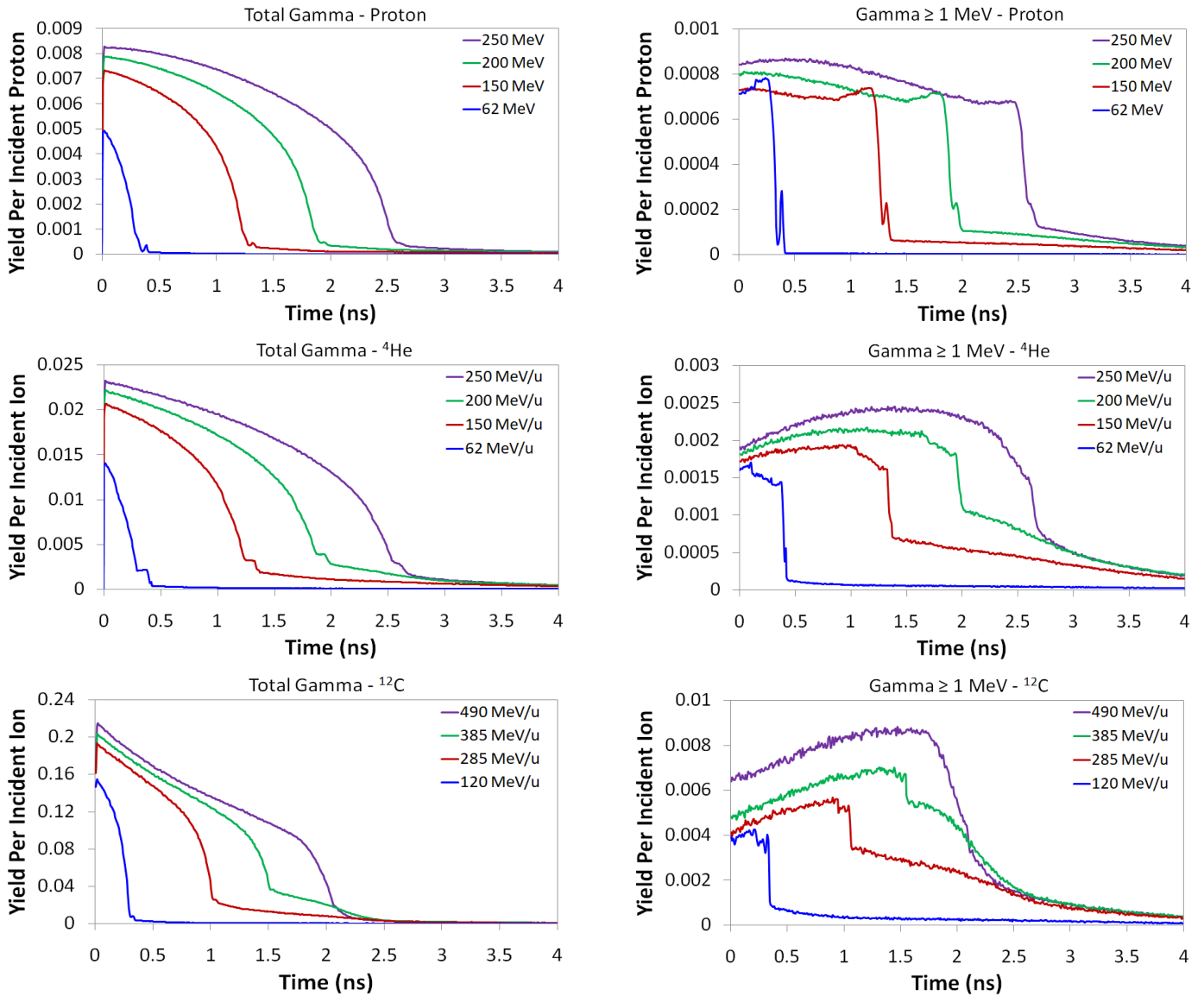


Figure 5. Emission time distribution of total gamma rays (left) and gamma rays  $\geq 1$  MeV (right) originating in the phantom for protons,  $^4\text{He}$  and  $^{12}\text{C}$  ions. The bin width is 0.01 ns.

Figure 6 shows the TOF spectra of total gamma rays, neutrons and gamma rays  $\geq 1$  MeV that reach the detection sphere once emitted from the phantom. As the beam energy increases, the PG TOF peak mean is seen to shift to longer TOF values while the peak width/integral increases. Again, this is attributed to the greater distance of travel by the ions in the phantom. For proton beams, neutrons are not predominantly detected until around 3 ns, which could suggest another means of discriminating PG rays from the background and hence improve the signal-to-background ratio of PG detection. This may be slightly more difficult for heavier ions helium and carbon particularly at high beam energies, for which there is a greater presence of neutron emission and temporal overlap between PG and neutrons.



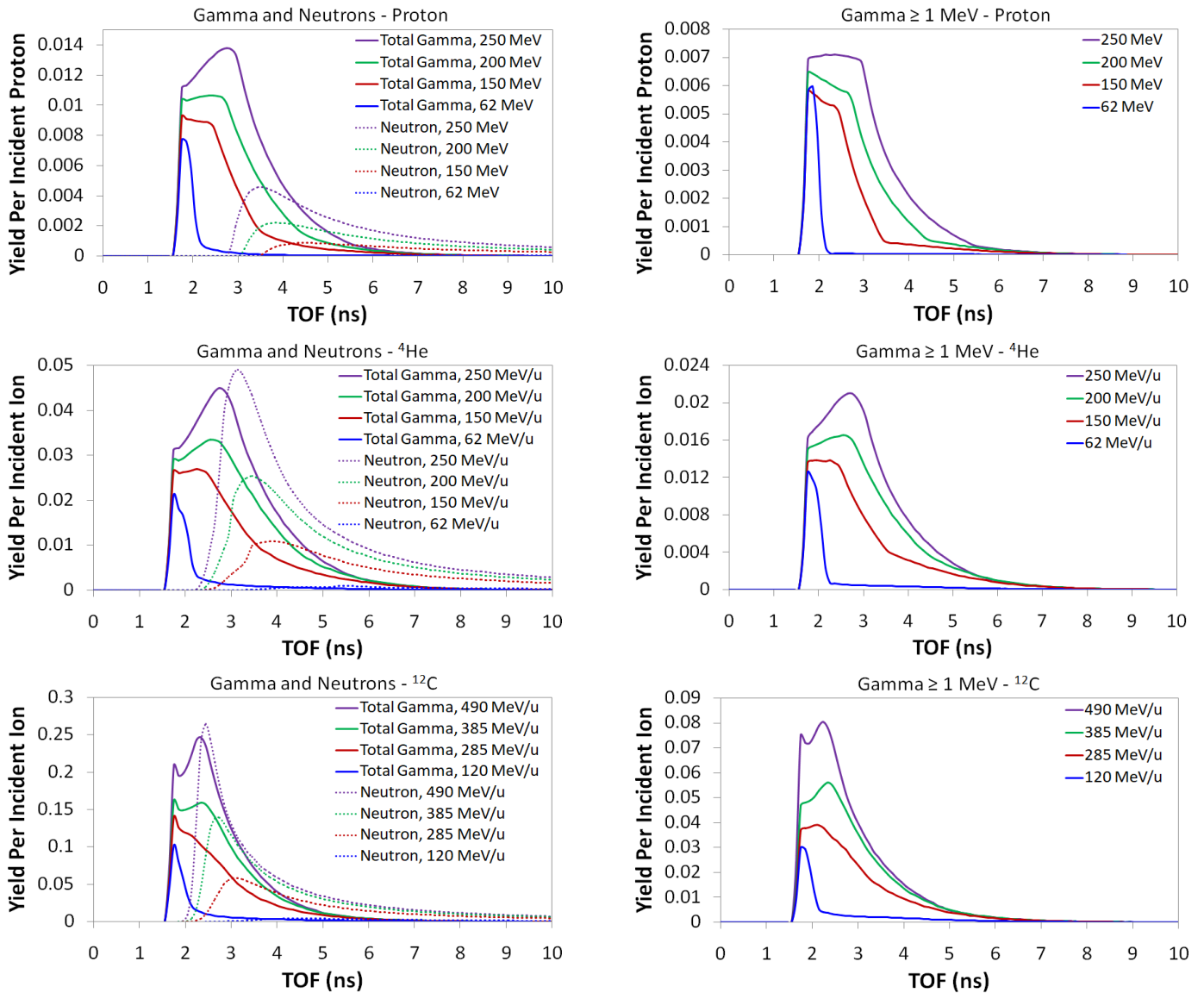


Figure 6. TOF spectra of total gamma and neutrons (left) and gamma rays  $\geq 1$  MeV (right) reaching the detection sphere once emitted from the phantom for protons,  $^4\text{He}$  and  $^{12}\text{C}$  ions. The bin width is 0.1 ns.

Figure 7 shows 2D representations of the TOF spectra of primary gamma rays along the polar angle  $\theta$  for proton,  $^4\text{He}$  and  $^{12}\text{C}$  beams at each of the beam energies studied, respectively. Figure 8 shows the same data for primary gamma rays  $\geq 1$  MeV. PG detection is seen to be increasingly forward-peaked, with respect to the phantom surface, with increasing beam energy for each particle beam type, as observed also in Figure 4. In addition, the TOF width increases and its maximum shifts to longer time values, particularly for proton and helium ions, whereas the TOF data for carbon irradiations shows less widening/shift in the distribution with greater local increase in PG yield. With additionally applying an energy threshold of 1 MeV to the primary gamma rays reaching the idealized detecting sphere, the TOF tail is seen to be almost entirely eliminated, leaving only the highly localized TOF peak.

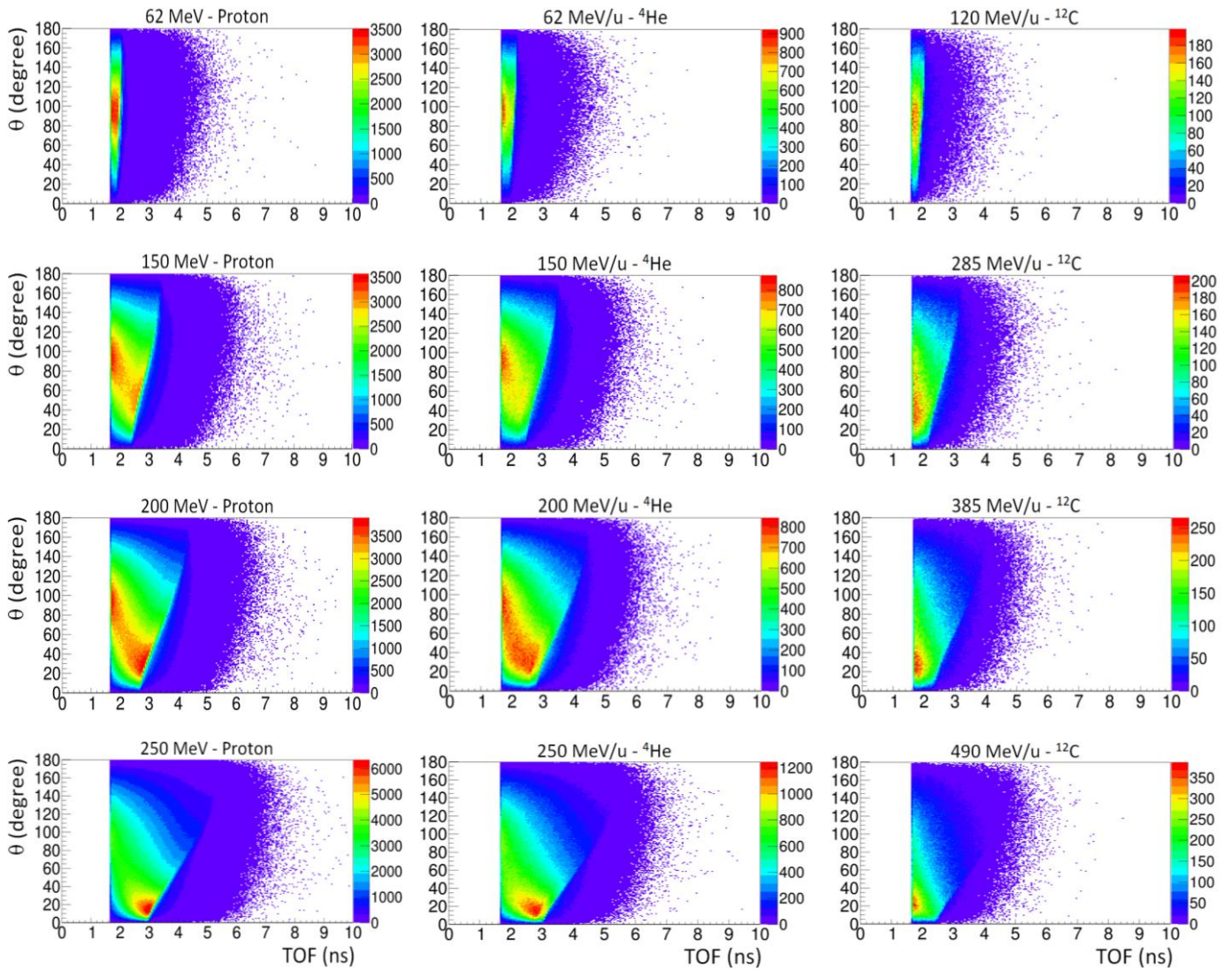
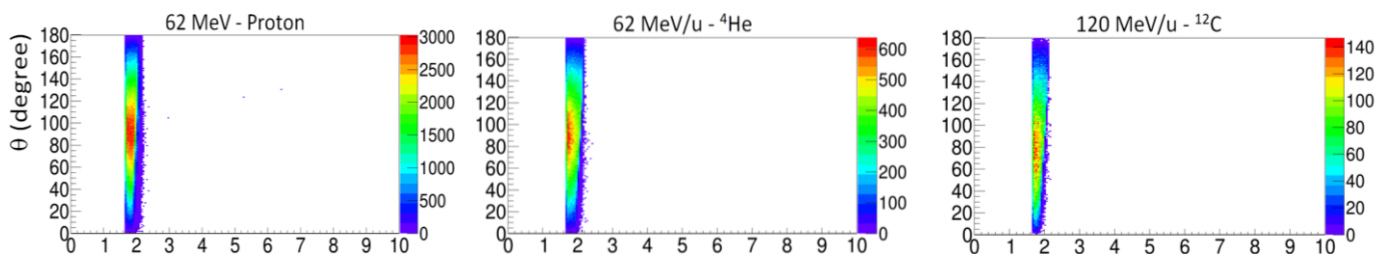


Figure 7. TOF spectra along the polar angle  $\theta$  of primary gamma rays reaching the detection sphere once emitted from the phantom for protons,  $^4\text{He}$  and  $^{12}\text{C}$  ions.



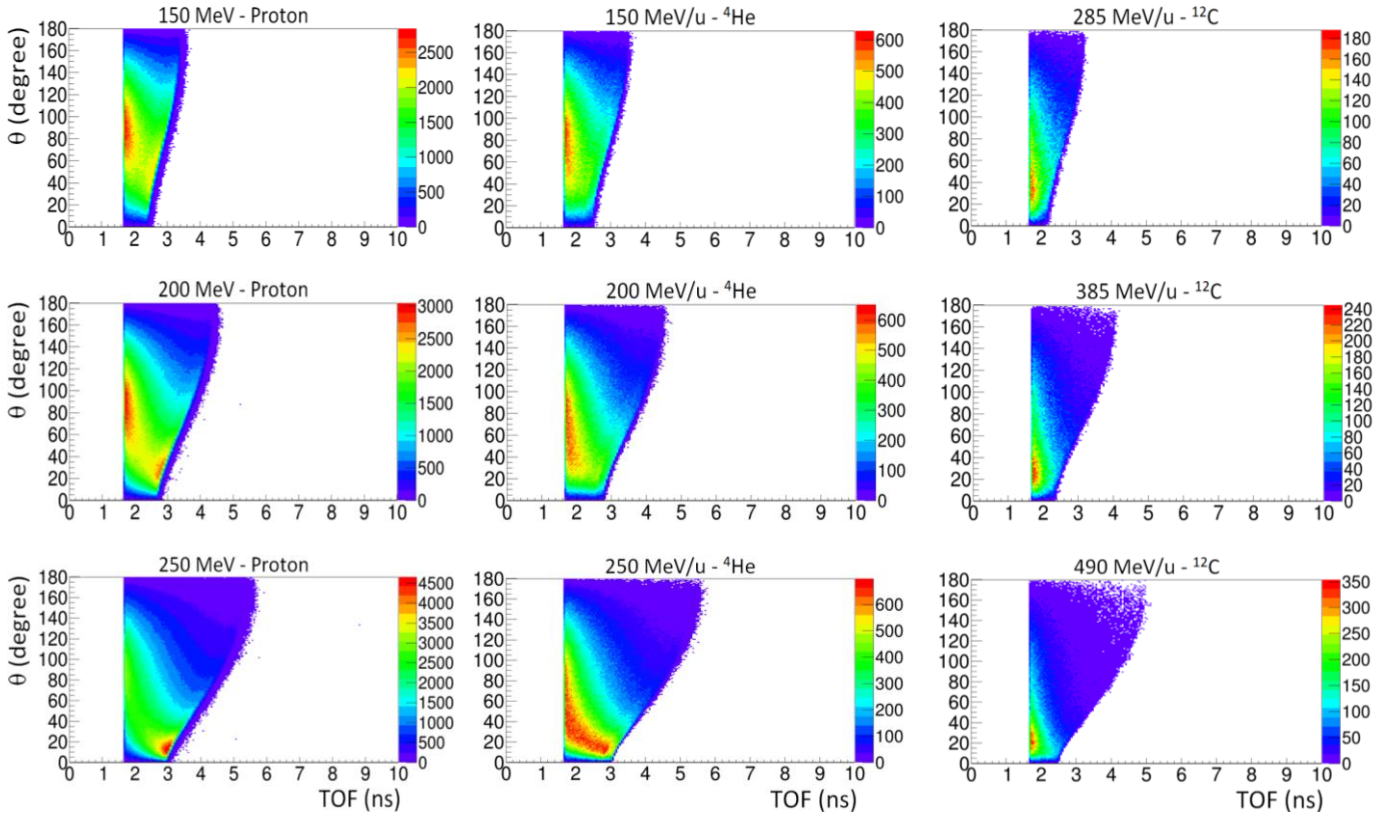
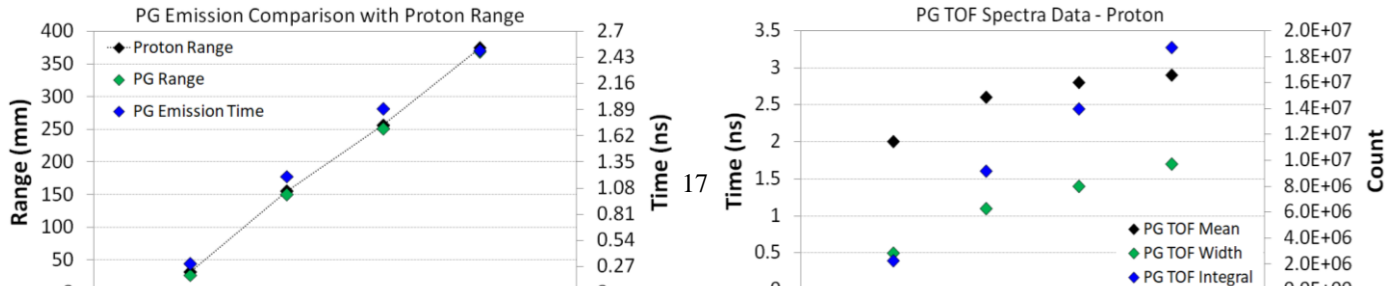


Figure 8. TOF spectra along the polar angle  $\theta$  of primary gamma rays  $\geq 1$  MeV reaching the detection sphere once emitted from the phantom for protons,  $^4\text{He}$  and  $^{12}\text{C}$  ions.

Figure 9 shows the particle beam range plotted against the PG range  $R_{\text{PG}}$  and PG emission time  $T_{\text{PG}}$ , as well as PG TOF data (peak mean, width and integral) for each particle type and energy studied. The PG data are those above the energy threshold of 1 MeV. As also seen in Section 3.2, the PG range offers good correlation with the particle range.  $T_{\text{PG}}$  values show a linear increase with beam energy, as the emission time of PG rays is correlated to the beam transit time and thus beam range. For a global detection setup, the PG TOF peak mean and width are found to only slightly increase with beam energy, with a minor drop in the case of carbon ions at higher energies. On the other hand, the PG TOF peak integral values exhibit a greater linear increase with particle beam energy.



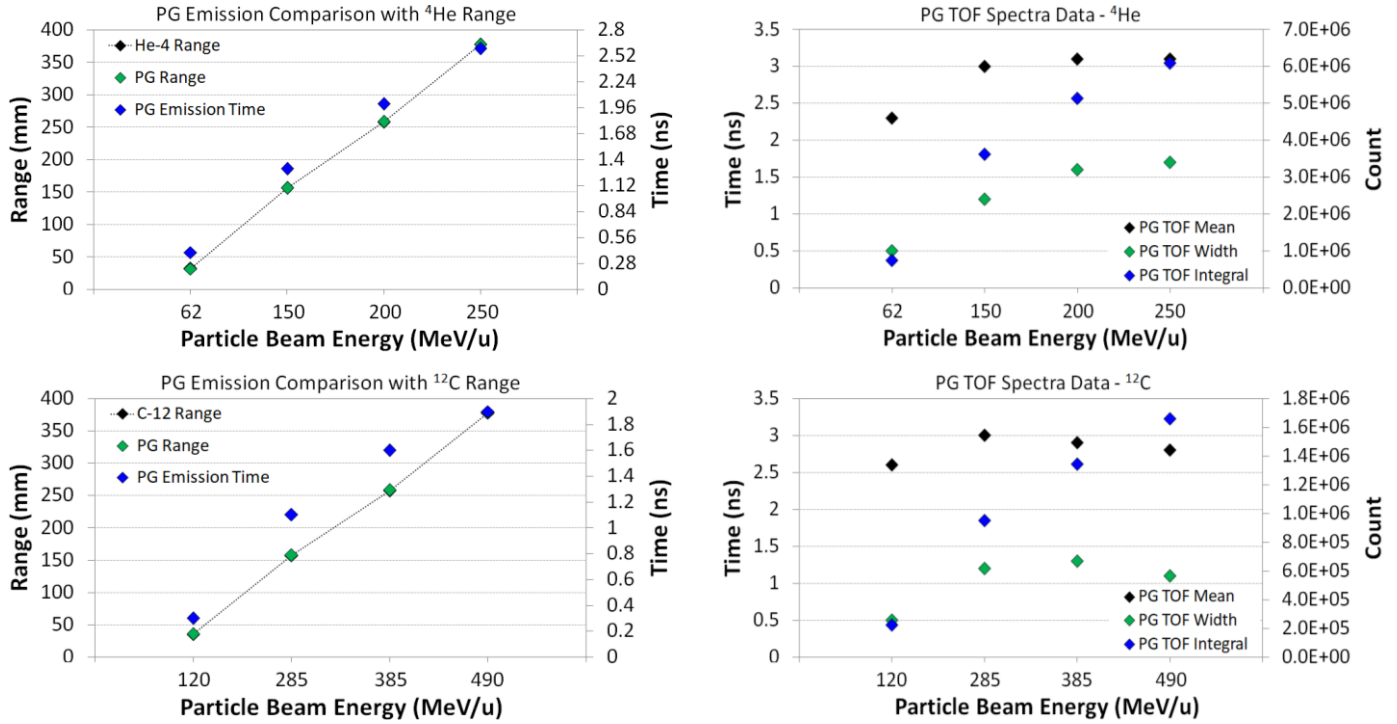


Figure 9. Quantitative comparison of the particle beam range with PG emission and detection data, for protons (top),  $^4\text{He}$  (centre) and  $^{12}\text{C}$  (bottom) ions. Left: Particle beam range and corresponding PG range  $R_{\text{PG}}$ , with PG emission time  $T_{\text{PG}}$ . The dotted line joining the particle range values serves to guide the eye. Right: PG TOF peak mean, width and integral. All PG data are for gamma rays  $\geq 1$  MeV. The uncertainty in the beam range is 0.5 mm, PG range is 0.1 mm, emission time/TOF mean is 0.1 ns, and TOF width is 0.2 ns.

#### 4. Discussion

In this work, the PG emission characteristics in the aspects of space, energy and time were investigated using Geant4 simulations with a water phantom irradiated with three different particle types: protons,  $^4\text{He}$  and  $^{12}\text{C}$  ions of varying energy. The PG production and detectable yields, energy spectral, spatial and temporal correlation characteristics with the depth dose profile were quantified. A relatively low energy threshold of 1 MeV for PG selection was used in this study to ensure higher statistics. For comparison, the PG energy window of 3.0-7.0 MeV adopted in other studies [50,51] was also included in our study.

Our results show that the primary PG emissions from the beam's nuclear interactions exhibit the closest correlation to the depth dose profile with sharp fall-off in the BP region, which is best suited for BP tracking in HT. The PG-BP correlations are better for heavier ions  $^4\text{He}$  and  $^{12}\text{C}$  than proton beams. The largest fall-off differences of PG production (comparing the applied energy selections) and the BP was found to be  $(6.2 \pm 0.5)$  mm for protons,  $(0.4 \pm 0.5)$  mm for  $^4\text{He}$  and  $(1.2 \pm 0.5)$  mm for  $^{12}\text{C}$  ions. A

consistent correlation in the lateral spreads between the PG emission and dose deposition is also observed in our study. These indicate that the PG signal is a reliable means for *in vivo* beam range verification and dose monitoring in HT. However, the measurable PG signal is largely masked by the concurrent emission of secondary PG rays resulting from the nuclear reactions undergone by the secondary particles/fragments created along the primary ion beam path since the primary PG and the secondary PG are not quite differentiable in experimental measurements. The secondary PG emissions with broad distribution and long tail beyond the BP region become more dominant in heavier ions (helium and carbon) than that in proton beams. This indicates that employing PG rays for range verification in carbon therapy presents more challenges.

With the use of an idealized detection sphere, the global angular distribution of detectable PG rays was investigated, for each particle type and energy studied. The observed non-isotropic longitudinal distribution of the detectable PG rays is likely due to the kinematics of the nuclear reactions. The default cascade model of Geant4 physics was used in our simulation study, which does not take angular momentum coupling of the gamma quanta emitted in a cascade into account. Further investigation is required to determine the influence of activating angular momentum coupling on the angular distribution. Attenuation/absorption of gamma rays within the phantom was taken into account in our simulation. So the geometric effect, such as the phantom shape and size, also play a role in the angular variances seen on the idealized detecting sphere. In replacing the sphere phantom with a box and cylinder phantom, we have observed that the shape of the phantom does have a considerable effect on the angular distribution due to attenuation/absorption. Additionally, since the target is not in the centre of the detection sphere, this introduces a dependency from the origin of the PG rays with  $1/r^2$ . These factors may be the reasons that our results of angular distribution are different to the experimental data in [23]. Hence, further study of the factors influencing the angular distribution of the detectable PG rays is necessary.

In addition to the changing angular distribution, the TOF distribution of gamma rays reaching the detection sphere also varies; the width and integral increase while the peak mean shifts to longer time values, which are also attributed by the greater distance of travel by the ions in the phantom. For primary gamma rays reaching the detecting sphere these angular/TOF properties are also seen, and with additionally applying an energy threshold of 1 MeV to the primary gamma rays, the TOF tail becomes almost entirely eliminated, leaving only the highly localized TOF peak. The detectable yield of high-energy PG rays was found to be about 65-70%. An important issue is whether there is enough PG statistics for spot tracking in PBS of HT. Considering a typical PBS proton beam with a rate of  $10^8$  protons per second and a spot duration of about 20 ms, each spot will have  $2 \times 10^6$  incident protons. If we consider our simulated beam incidence as a single spot, for  $2 \times 10^6$  incident protons at 150 MeV the total detectable PG yield at energy  $\geq 1$  MeV on the idealized detecting sphere would be  $\sim 1.8 \times 10^5$  with a production yield of  $\sim 2.6 \times 10^5$  within the water phantom. Considering a  $5 \times 5$  cm<sup>2</sup> detector size on the simulated sphere the detectable PG counts are  $\sim 3 \times 10^2$ , yielding a statistical error of about 6%. This implies that spot by spot monitoring using PG rays for this particular beam



energy/geometry/detector size is a challenge in terms of obtaining sufficient statistics for clinical applications in HT. As mentioned by Krimmer et al 2018 [19], the statistics can be increased by accumulating the information from several beam spots when they correspond to the same expected range, but at the expense of spatial resolution. In comparison, our results show that  $^{12}\text{C}$  ions provide a higher PG yield; for  $2 \times 10^6$  incident ions, which corresponds to around 69 MeV/ion deposited energy at the BP position, at 285 MeV/u the detectable PG counts are  $\sim 3 \times 10^3$  on a  $5 \times 5 \text{ cm}^2$  detector size. Similarly, for  $2 \times 10^6$  incident  $^4\text{He}$  ions at 150 MeV/u the detectable PG counts on a  $5 \times 5 \text{ cm}^2$  area is  $\sim 1 \times 10^3$ .

The temporal characteristics of PG rays were also studied in terms of the PG emission time within the phantom and PG detection time at the idealized detecting sphere, with the beam incidence marking the start time. The PG emission time is associated with the beam transit time which is closely correlated to the depth of beam interaction in matter. So the beam range can be extracted from the measured TOF spectrum of PG rays as well. The PGT [35] method retrieves the beam range by means of the TOF peak's mean and width while the PGPI [36] method makes use of the integral counts of the TOF spectrum to extract the beam range. With the idealized detection sphere, the obtained PG TOF spectrum is most likely to reflect the intrinsic characteristics of the PG TOF spectroscopy from the phantom. The realistic PG TOF spectrum in experimental measurements could be much more complicated and it largely depends on the nature of the delivered beam time structure and also the detector's time resolution [54]. The very narrow time range of PG TOF in a few nanoseconds implies that ultra-high time resolution of the detector ( $< 1 \text{ ns}$ ) is required in order to accurately extract the range information from the measured PG TOF spectroscopy. In addition, the good separation in the TOF characteristics between PG rays and neutrons can be utilized to discriminate the PG signal from the neutrons and neutron-associated backgrounds. This has been proposed by Testa et al 2008 [55] for  $^{12}\text{C}$  ions at low energies where the radiofrequency (RF) signal of the accelerator at the GANIL facility could be used as the start time reference. However, this technique is not suitable for synchrotron facilities, where instead a trigger signal from a fast transmission detector may be used. Biegun et al 2012 [56] used Monte Carlo simulations to investigate the TOF neutron rejection technique for protons. Hueso-González et al 2018 [37] performed experimental measurements of the technique for protons accelerated by cyclotrons. However, the application of TOF for proton,  $^4\text{He}$  and  $^{12}\text{C}$  ions in synchrotron facilities at clinical energies and intensities has not yet been demonstrated experimentally. As pointed out in [19], TOF may be inefficient for PG detection in proton therapy with synchrotrons due to long bunch times, while for carbon therapy the detection of individual ion impacts may be possible at mean intensities of  $10^7$ - $10^8$  ions/second by means of fast beam hodoscopes. Combining the TOF and angular preference of PG detections could further improve the signal-to-background ratio for PG measurements.

## 5. Conclusion

The PG signal is a reliable means for *in vivo* range verification via BP tracking in HT. The primary PG rays exhibit the closest correlation to the beam range but it is masked by the concurrent secondary PG rays. The dominant secondary PG rays in heavier ions such as carbon beams impose greater challenges for BP tracking from the PG profile. The investigation into the angular distribution of PG rays showed a changing angular propagation distribution with beam energy, which may suggest that a movable PG detector coordinated with respect to the beam range could serve to optimize the detection efficiency of PG rays. The influence of activating angular momentum coupling on the angular distribution has not been investigated in this study but we will quantify the coupling effect in the next stage of this work. The PG TOF spectroscopy encodes the essential information of the beam range but needs high time resolution measurements to retrieve it. Hybrid PG detection systems to utilize the energy, timing and spatial characteristics of PG rays is desirable for BP tracking in real-time.

## Acknowledgements

This research has been conducted with the support of the Australian Government Research Training Program Scholarship.

We would like to thank the University of Wollongong Information Management & Technology Services (IMTS) for computing time on the UOW High Performance Computing Cluster.

The authors would like to thank Vladimir Ivantchenko and Laurent Desorgher of the Geant4 Collaboration for their valuable help in discussion on the Geant4 modelling of the nuclear de-excitation.

## References

- [1] Durante M, Paganetti H. Nuclear physics in particle therapy: a review. *Rep. Prog. Phys.* 2016;79:096702.
- [2] Schardt D, Elsässer T, Schulz-Ertner D. Heavy-ion tumor therapy: physical and radiobiological benefits. *Rev. Mod. Phys.* 2010;82:383-425.
- [3] Lomax AJ. Intensity modulated proton therapy and its sensitivity to treatment uncertainties 1: the potential effects of calculational uncertainties. *Phys. Med. Biol.* 2008;53:1027-42.
- [4] Paganetti H. Range uncertainties in proton therapy and the role of Monte Carlo simulations. *Phys. Med. Biol.* 2012;57:R99-R117.
- [5] Henriquet P, Testa E, Chevallier M, Dauvergne D, Dedes G, Freud N, et al. Interaction vertex imaging (IVI) for carbon ion therapy monitoring: a feasibility study. *Phys. Med. Biol.* 2012;57:4655-69.
- [6] Yamaguchi M, Nagao Y, Ando K, Yamamoto S, Toshito T, Kataoka J, et al. Secondary-electron-bremsstrahlung imaging for proton therapy. *Nucl. Instrum. Methods Phys. Res.* 2016;A833:199-207.
- [7] Assmann W, Kellnberger S, Reinhardt S, Lehrack S, Edlich A, Thirolf PG, et al. Ionoacoustic characterization of the proton Bragg peak with submillimeter accuracy. *Med. Phys.* 2015;42:567-74.
- [8] Polf JC, Parodi K. Imaging particle beams for cancer treatment. *Phys. Today* 2015;68:28-33.
- [9] Knopf AC, Lomax A. *In vivo* proton range verification: a review. *Phys. Med. Biol.* 2013;58:131-60.
- [10] Kraan AC. Range verification methods in particle therapy: underlying physics and Monte Carlo modelling. *Front Oncol.* 2015;5:150.
- [11] Oelfke U, Lam GK, Atkins MS. Proton dose monitoring with PET: quantitative studies in Lucite. *Phys. Med. Biol.* 1996;41:177-96.
- [12] Parodi K, Enghardt W. Potential application of PET in quality assurance of proton therapy. *Phys. Med. Biol.* 2000;45:N151-56.
- [13] Parodi K, Paganetti H, Shih HA, Michaud S, Loeffler JS, DeLaney TF, et al. Patient study of *in vivo* verification of beam delivery and range, using positron emission tomography and computed tomography imaging after proton therapy. *Int. J. Radiat. Oncol. Biol. Phys.* 2007;68:920-34.

- [14] Moteabbed M, España S, Paganetti H. Monte Carlo patient study on the comparison of prompt gamma and PET imaging for range verification in proton therapy. *Phys. Med. Biol.* 2011;56:1063-82.
- [15] Min CH, Kim CH, Youn MY, Kim JW. Prompt gamma measurements for locating the dose falloff region in the proton therapy. *Appl. Phys. Lett.* 2006;89:183517.
- [16] Polf JC, Peterson S, Ciangaru G, Gillin M, Beddar S. Prompt gamma-ray emission from biological tissues during proton irradiation: a preliminary study. *Phys. Med. Biol.* 2009;54:731-43.
- [17] Testa E, Bajard M, Chevallier M, Dauvergne D, Le Foulher F, Freud N, et al. Dose profile monitoring with carbon ions by means of prompt-gamma measurements. *Nucl. Instrum. Methods Phys. Res.* 2009;B267:993-6.
- [18] Pinto M, Bajard M, Brons S, Chevallier M, Dauvergne D, Dedes G, et al. Absolute prompt-gamma yield measurements for ion beam therapy monitoring. *Phys. Med. Biol.* 2015;60:565-94.
- [19] Krimmer J, Dauvergne D, Létang JM, Testa É. Prompt-gamma monitoring in hadrontherapy: A review. *Nucl. Instrum. Methods Phys. Res.* 2018;A878:58-73.
- [20] Tommasino F, Scifoni E, Durante M. New Ions for Therapy. *Int. J. Particle Ther.* 2015;428-38. doi: 10.14338/IJPT-15-00027.1.
- [21] Krämer M, Scifoni E, Schuy C, Rovituso M, Tinganelli W, Maier A, et al. Helium ions for radiotherapy? Physical and biological verifications of a novel treatment modality. *Med. Phys.* 2016;43:1995-2004.
- [22] Tessonnier T, Mairani A, Brons S, Haberer T, Debus J, Parodi K. Experimental dosimetric comparison of  $^1\text{H}$ ,  $^4\text{He}$ ,  $^{12}\text{C}$  and  $^{16}\text{O}$  scanned ion beams. *Phys. Med. Biol.* 2017;62:3958-82.
- [23] Mattei I, Bini F, Collamati F, De Lucia E, Frallicciardi PM, Iarocci E, et al. Secondary radiation measurements for particle therapy applications: prompt photons produced by  $^4\text{He}$ ,  $^{12}\text{C}$  and  $^{16}\text{O}$  ion beams in a PMMA target. *Phys. Med. Biol.* 2017;62:1438-55.
- [24] Bom V, Joulaeizadeh L, Beekman FJ. Real-time prompt gamma monitoring in spot-scanning proton therapy using imaging through a knife-edge-shaped slit. *Phys. Med. Biol.* 2012;57:297-308.
- [25] Smeets J, Roellinghoff F, Prieels D, Stichelbaut F, Benilov A, Busca P, et al. Prompt gamma imaging with slit camera for real-time range control in proton therapy. *Phys. Med. Biol.* 2012;57:3371-405.
- [26] Perali I, Celani A, Bombelli L, Fiorini C, Camera F, Clementel E, et al. Prompt gamma imaging of proton pencil beams at clinical dose rate. *Phys. Med. Biol.* 2014;59:5849-71.
- [27] Peterson SW, Robertson D, Polf J. Optimizing a three-stage Compton camera for measuring prompt gamma rays emitted during proton radiotherapy. *Phys. Med. Biol.* 2010;55:6841-56.
- [28] Richard MH, Chevallier M, Dauvergne D, Freud N, Henriquet P, Le Foulher F, et al. Design guidelines for a double scattering Compton camera for prompt- $\gamma$  imaging during ion beam therapy: a Monte Carlo simulation study. *IEEE Trans. Nucl. Sci.* 2011;58:87-94.
- [29] Kormoll T, Fiedler F, Schöne S, Wüstemann J, Zuber K, Enghardt W. A Compton imager for in-vivo dosimetry of proton beams – A design study. *Nucl. Instrum. Methods Phys. Res.* 2011;626-627:114-9.
- [30] Richter C, Pausch G, Barczyk S, Priegnitz M, Keitz I, Thiele J, et al. First clinical application of a prompt gamma based in vivo proton range verification system. *Radiother. Oncol.* 2016;118:232-7.
- [31] Xie Y, Bentefour EH, Janssens G, Smeets J, Stappen FV, Hotoiu L, et al. Prompt gamma imaging for in vivo range verification of pencil beam scanning proton therapy. *Int. J. Radiat. Oncol. Biol. Phys.* 2017;99:210-8.
- [32] Rohling H, Priegnitz M, Schoene S, Schumann A, Enghardt W, Hueso-González F, et al. Requirements for a Compton camera for in vivo range verification of proton therapy. *Phys. Med. Biol.* 2017;62:2795-811.
- [33] Verburg JM, Seco J. Proton range verification through prompt gamma-ray spectroscopy. *Phys. Med. Biol.* 2014;59:7089-106.
- [34] Kelleter L, Wrońska A, Besuglow J, Konefał A, Laihem K, Leidner J et al. Spectroscopic study of prompt-gamma emission for range verification in proton therapy. *Phys. Med.* 2017;34:7-17.
- [35] Golnik C, Hueso-González F, Müller A, Dendooven P, Enghardt W, Fiedler F, et al. Range assessment in particle therapy based on prompt gamma-ray timing measurements. *Phys. Med. Biol.* 2014;59:5399-422.
- [36] Krimmer J, Angellier G, Balleyguier L, Dauvergne D, Freud N, Hérault J, et al. A cost-effective monitoring technique in particle therapy via uncollimated prompt gamma peak integration. *Appl. Phys. Lett.* 2017;110:154102.
- [37] Hueso-González F, Rabe M, Ruggieri T, Bortfeld T, Verburg JM. A full-scale clinical prototype for proton range verification using prompt gamma-ray spectroscopy. *Phys. Med. Biol.* 2018;63:185019. doi: 10.1088/1361-6560/aad513.
- [38] Agostinelli S, Allison J, Amako K, Apostolakis J, Araujo H, Arce P, et al. Geant4—a simulation toolkit. *Nucl. Instrum. Methods Phys. Res.* 2003;A506:250-303.
- [39] Allison J, Amako K, Apostolakis J, Araujo H, Arce P, Asai M, et al. Geant4 developments and applications. *IEEE Trans. Nucl. Sci.* 2006;53:270-8.
- [40] Allison J, Amako K, Apostolakis J, Arce P, Asai M, Aso T, et al. Recent developments in Geant4. *Nucl. Instrum. Methods Phys. Res.* 2016;A835:186-225.
- [41] National Institute of Standards and Technology (NIST). Stopping-Power & Range Tables for Electrons, Protons, and Helium Ions. <https://www.nist.gov/>
- [42] Ziegler JF, Ziegler MD, Biersack JP. The Stopping and Range of Ions in Matter (SRIM). *Nucl. Instrum. Methods Phys. Res.* 2010;B268:1818-23. doi: 10.1016/j.nimb.2010.02.091. <http://www.srim.org/>



- [43] Jarlskog CZ, Paganetti H. Physics settings for using the Geant4 toolkit in proton therapy. *IEEE Trans. Nucl. Sci.* 2008;55:1018-25.
- [44] Bolst D, Cirrone GAP, Cuttone G, Folger G, Incerti S, Ivanchenko V, et al. Validation of Geant4 fragmentation for heavy ion therapy. *Nucl. Instr. Meth. Phys. Res.* 2017;869:68-75.
- [45] Grichine VM. A simplified Glauber model for hadron-nucleus cross sections. *Eur. Phys. J. C* 2009;62:399-404. doi: 10.1140/epjc/s10052-009-1033-z.
- [46] Folger G, Wellisch J, Ivanchenko VN. The binary cascade: Nucleon nuclear reactions. *Eur. Phys. J. A* 2004;21:407-17.
- [47] Dedes G, Pinto M, Dauvergne D, Freud N, Krimmer J, Létang JM, et al. Assessment and improvements of Geant4 hadronic models in the context of prompt-gamma hadrontherapy monitoring. *Phys. Med. Biol.* 2014;59:1747-72.
- [48] Vanstalle M, Mattei I, Sarti A, Bellini F, Bini F, Collamati F, et al. Benchmarking Geant4 hadronic models for prompt- $\gamma$  monitoring in carbon ion therapy. *Med. Phys.* 2017;44:4276-86.
- [49] Krimmer J, Chevallier M, Constanzo J, Dauvergne D, De Rydt M, Dedes G, et al. Collimated prompt gamma TOF measurements with multi-slit multi-detector configurations. *JINST.* 2015;10:P01011. doi: 10.1088/1748-0221/10/01/P01011.
- [50] Lopes PC, Clementel E, Crespo P, Henrotin S, Huizenga J, Janssens G, et al. Time-resolved imaging of prompt-gamma rays for proton range verification using a knife-edge slit camera based on digital photon counters. *Phys. Med. Biol.* 2015;60:6063-85.
- [51] Schumann A, Petzoldt J, Dendooven P, Enghardt W, Golnik C, Hueso-González F, et al. Simulation and experimental verification of prompt gamma-ray emissions during proton irradiation. *Phys. Med. Biol.* 2015;60:4197-207.
- [52] Kozlovsky B, Murphy RJ, Ramaty R. Nuclear deexcitation gamma-ray lines from accelerated particle interactions. *Astrophys. J. Suppl. Ser.* 2002;141:523-41.
- [53] Zarifi M, Guatelli S, Bolst D, Hutton B, Rosenfeld A, Qi Y. Characterization of prompt gamma-ray emission with respect to the Bragg peak for proton beam range verification: A Monte Carlo study. *Phys. Med.* 2017;33:197-206.
- [54] Hueso-González F, Enghardt W, Fiedler F, Golnik C, Janssens G, Petzoldt J, et al. First test of the prompt gamma ray timing method with heterogeneous targets at a clinical proton therapy facility. *Phys. Med. Biol.* 2015;60:6247-72.
- [55] Testa E, Bajard M, Chevallier M, Dauvergne D, Le Foulher F, Freud N, et al. Monitoring the Bragg peak location of 73 MeV/u carbon ions by means of prompt  $\gamma$ -ray measurements. *Appl. Phys. Lett.* 2008;93:093506.
- [56] Biegun AK, Seravalli E, Lopes PC, Rinaldi I, Pinto M, Oxley DC, et al. Time-of-flight neutron rejection to improve prompt gamma imaging for proton range verification: a simulation study. *Phys. Med. Biol.* 2012;57:6429-44.